Composites Part A 108 (2018) 41–52

Contents lists available at ScienceDirect

Composites Part A

journal homepage: www.elsevier.com/locate/compositesa

Permeability and capillary effects in a channel-wise non-crimp fabric

Damiano Salvatori, Baris Caglar, Helena Teixidó, Véronique Michaud*

Laboratory for Processing of Advanced Composites (LPAC), Institute of Materials (IMX), Ecole Polytechnique Fédérale de Lausanne (EPFL), Station 12, 1015 Lausanne, Switzerland

ARTICLE INFO

Keywords:
A. Fabrics/textiles
B. Permeability
E. Liquid composite moulding
E. Fibre tow infiltration

ABSTRACT

Flow properties are investigated for a non-crimp glass fabric with large meso-channels designed for high-permeability, as compared to glass twill woven fabric. Saturated and unsaturated permeability are measured through in-plane, unidirectional, constant-pressure flow experiments. Capillary effects are evaluated following a novel approach based on the ratio of unsaturated and saturated permeability for a set of experiments conducted at capillary numbers varying over a large range from $\sim 4{\cdot}10^{-5}$ to $4{\cdot}10^{-1}$. The mesoscopic pore-space of the compacted fabrics is imaged with X-ray Tomography, and analyzed to propose permeability predictions based on the channels geometry, which correspond well to experimental results. Permeability is governed by viscous flow in the meso-channels. As a result, provided that the capillary number exceeds a threshold value, the permeability can be rather accurately measured in these dual-scale fabrics by carrying out unsaturated measurements, neglecting micro-flow and capillary effects.

1. Introduction

Liquid Composite Molding (LCM) is a class of manufacturing processes for continuous fiber reinforced composites which consists in the direct impregnation of a stack of fabric layers placed in a mold with a liquid resin prior to reticulation or solidification of the resin phase. To reach medium to high volume production of parts, or allow production of large parts, it is desired to keep this impregnation step as short as possible, while ensuring a complete filling of the part. Poor impregnation results in residual porosity of the matrix which negatively affects the final properties of the part [1,2]. Part quality and process time are ultimately related to processing conditions and properties of both resin (e.g. viscosity and surface tension) and fabric (e.g. architecture and permeability). Permeability is a measure of the inverse of the resistance that a porous medium opposes to fluid flow, and it is strongly related to porosity (i.e. to fibers volume fraction for a fibrous preform). Typical glass and carbon fabrics have permeability values in the order of 10^{-10} to 10^{-13} m^2 for fiber volume fractions between 40% and 60%. Such small values restrict the application of LCM to low-viscosity resins (<1 Pa s), as is the case of most reactive formulations for thermoset and thermoplastic matrices. Resins with higher viscosity (e.g. high-fluidity thermoplastics in the melt state) require higher permeability ($\sim 10^{-9}$) in order to fully impregnate a small part (<20 cm) in a reasonable time (<5 min). Therefore, enhancement of fabric permeability without reducing the fiber volume fraction, necessary for structural performance, is a major goal for fabric manufacturers as well as a scientific challenge.

Many studies show that fiber surface morphology and fabric architecture dramatically affect permeability [3–9]. In particular, the number, shape and size of meso-channels along the flow direction can be exploited to significantly enhance in-plane permeability [6,8,9].

However, the resulting dual peak porosity distribution in the fabric (i.e. the micro-pores in the intra-tow space and the macro-pores in the inter-tow space) lead to dual-scale flow and risk of void entrapment during fabric impregnation [10–18]. If capillary forces are high compared to viscous forces, micro-flow will dominate and macro-voids can be trapped in the inter-tow spaces. Conversely, if capillary forces are negligible, flow in the inter-tow space is dominant and micro-voids can be trapped within the intra-tow spaces. Previous studies indicated that voids can be minimal when the flow velocity corresponds to an equilibrium point between capillary and viscous forces [10,11,14–17]. For this reason, the capillary number, defined as the ratio between viscous and capillary forces, that is

$$Ca = \frac{v\eta}{\gamma_a} \tag{1}$$

where η,γ_a and v are respectively the fluid viscosity, surface tension in air and velocity, is considered. The optimal Ca value should be that for which capillary and viscous forces compensate, resulting in comparable flow velocities in the inter- and intra-tow regions, which leads to a minimum void content in the final part [11,14–17].

Capillary effects are also considered to be responsible for discrepancies between permeability measured from the flow front position

* Corresponding author.
E-mail address: veronique.michaud@epfl.ch (V. Michaud).

https://doi.org/10.1016/j.compositesa.2018.02.015
Received 23 November 2017; Received in revised form 7 February 2018; Accepted 9 February 2018
Available online 15 February 2018
1359-835X/

during fabric impregnation (generally referred to as unsaturated permeability) and after full impregnation is complete (referred to as steady-state, or saturated, permeability). Fabric permeability stricto sensu is related to the porous medium architecture only and should be independent from the fluid properties and experimental conditions. In practice, several studies report large experimental scatter in permeability measurements, depending on measurement methods and fluid type [19–21]. Some authors investigated the influence of test fluids on measured permeability, apparently with different results [22–24]. Hammond and Loos [23] did not report any significant differences in permeability for both a glass fabric (plain weave) and a carbon fabric (8-harness satin) measured with corn oil, water or epoxy resin. Moreover, they obtained similar results for saturated and unsaturated permeability. However, they investigated only a limited range of capillary numbers (roughly between 0.001 and 0.02). Steenkamer et al. [22] reported a large dependence of permeability on fluid type (vinyl ester resin, motor oil and corn syrup were used), and related it to capillary effects.

The objectives of the present work are to study the permeability of a fabric with large dual-scale effects with varying capillary number and to develop a novel model for permeability prediction based on the geometry of the meso-channels. In particular, we studied both saturated and unsaturated permeability of a non-crimp fabric which has a pronounced dual-scale architecture, along with a reference woven fabric. The particular structure of this non-crimp fabric is responsible for fast flow in one direction, and is designed for impregnation with viscous fluids and flow at high capillary number (>0.1). As an example, this fabric is suitable for long-range impregnation with molten thermoplastics, allowing for novel manufacturing strategies of thermoplastic composite components [25]. Permeability measurements were conducted over a wide range of capillary numbers (between $4{\cdot}10^{-5}$ and $4{\cdot}10^{-1}$) using different fluids, in order to evaluate the role of capillary phenomena and their influence on flow front morphology. The meso-structure of the fabric preforms was analyzed from Computed X-ray Tomography images, from which a simple numerical permeability model was proposed. Finally, the generally observed discrepancy between unsaturated and saturated permeability was quantified and explained in light of the capillary number and fabric architecture.

2. Theoretical background

The resin filtration process is considered as flow of a Newtonian fluid in a porous medium (i.e. the dry fibrous reinforcement), which is driven by a pressure gradient throughout the porous medium itself. In combination with the mass conservation equation, Darcy's law is commonly used in LCM to describe this type of flow. For isothermal saturated flow in a rigid preform it takes the following expression:

$$v = -\frac{K}{\eta(1-V_f)}\nabla P \tag{2}$$

where v is the fluid velocity, η the fluid viscosity, V_f the volume fraction of fibers, ∇P the pressure gradient, and K is fabric permeability. For one-dimensional flow of an incompressible fluid under constant applied pressure at the mold inlet, assuming a slug-flow boundary condition at the flow front (i.e. fabric stack is either fully wet or fully dry) and neglecting capillary pressure drop at the flow front, pressure is found to decrease linearly along the impregnated portion of the fabric, i.e. between the mold inlet (P_i) and the flow front (P_f) (Fig. 1a). Therefore, at any moment during the impregnation, the pressure gradient can be expressed as

$$\nabla P = \frac{P_f - P_i}{L(t)} = \frac{\Delta P_{app}}{L(t)} < 0 \tag{3}$$

where $L(t)$ is the flow front position at time t. Pressure at the flow front P_f is assumed to be the pressure of the air in the dry fabric (typically atmospheric pressure). Thus, Eq. (2) becomes

$$\frac{dL(t)}{dt} = -\frac{K}{\eta(1-V_f)}\frac{\Delta P_{app}}{L(t)} \tag{4}$$

which after integration leads to

$$L^2(t) = -\frac{2K_{unsat}}{\eta(1-V_f)}\Delta P_{app}\, t. \tag{5}$$

From Eq. (5) follows that a measurement of the flow front position as a function of time, under constant-pressure impregnation allows an indirect measurement of permeability. In this case, it is referred to as unsaturated permeability, denoted as K_{unsat}. It is distinguished from the saturated permeability K_{sat}, which is measured from the flow rate at the outlet Q_{out}, after full impregnation has already taken place. In that case, Darcy's law is simply

$$\frac{Q_{out}}{A} = -\frac{K_{sat}}{\eta}\frac{\Delta P_{app}}{L_f} \tag{6}$$

where A is the cross-section area of the fabric stack and L_f its length. Ideally, K_{unsat} should be equal to K_{sat}. In practice, differences between the two values are often observed and object of study [24,26–28]. In particular, during unsaturated flow, additional forces related to capillary phenomena may play a role at the interface between the fluid front and the dry fabric. These can be modeled as a capillary pressure drop (ΔP_γ) localized at the flow front (Fig. 1b). The total pressure difference between inlet and outlet then becomes:

$$\Delta P = \Delta P_{app} + \Delta P_\gamma. \tag{7}$$

Capillary pressure drop depends on contact angle θ (the angle at the interface between fluid, glass fiber and air) according to [29]:

$$\Delta P_\gamma = -S_f \gamma_a \cos\theta, \tag{8}$$

where S_f is the area of matrix-fiber interface per unit volume of matrix and γ_a the surface tension in air of the fluid. When the fluid is moving at velocity v, the dynamic contact angle θ deviates from the static contact angle θ_0 according to Tanner's law [30]:

$$\theta^3 - \theta_0^3 = c_T Ca \tag{9}$$

where c_T is an experimental constant and Ca the capillary number (Eq. (1)). For a drop of fluid in contact with a surface, the fluid is defined as wetting if $\theta < 90°$ ($\Delta P_\gamma < 0$) or non-wetting if $\theta > 90°$ ($\Delta P_\gamma > 0$). Consequently, in the dynamic regime it is possible for a given liquid-solid system to be both wetting and non-wetting, depending on the liquid velocity. A transition from wetting to non-wetting flow when increasing the capillary number was demonstrated for epoxy flowing into a carbon non-crimp fabric [13].

Assuming that the difference between K_{unsat} and K_{sat} is attributed to capillary effects only, Eq. (5) replacing K_{unsat} by K_{sat} and ΔP_{app} by ΔP (Eq. (7)) becomes:

$$L^2(t) = -\frac{2K_{sat}}{\eta(1-V_f)}(\Delta P_{app} + \Delta P_\gamma)t. \tag{10}$$

Combining Eqs. (5) and (10), and defining R_s as the ratio of unsaturated-to-saturated permeability, the following relation is found:

$$R_s = \frac{K_{unsat}}{K_{sat}} = 1 + \frac{\Delta P_\gamma}{\Delta P_{app}}. \tag{11}$$

Following this approach, if capillary effects are negligible or absent ($|\Delta P_\gamma| \ll |\Delta P_{app}|$), R_s will be equal to 1, and K_{unsat} and K_{sat} values will coincide. If capillary effects are not negligible, the two permeability values will differ. In particular, the sign of the pressure drop will determine whether R_s is greater or smaller than 1. Typical values of capillary pressure in LCM range from few to tens of kPa [13,31,32], hence capillary effects may not be neglected, especially for infiltration conducted under very low applied pressure.

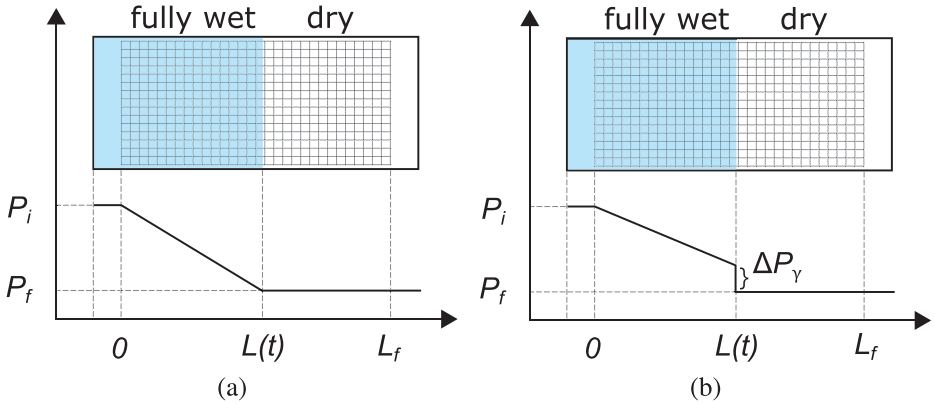

Fig. 1. Schema of impregnation showing the pressure profile along the fabric stack without (a) and with (b) the presence of capillary pressure drop at the flow front. (For interpretation of the references to colour in this figure legend, the reader is referred to the web version of this article.)

3. Materials and methods

3.1. Fabrics

Two types of glass fabric supplied by Chomarat™ have been employed in this study: a non-crimp fabric (NCF), G-PLY™, and a woven 2/2 twill, G-WEAVE™. G-PLY™ consists of highly densely packed fiber bundles (0°), which are stitched with a polyester yarn on a layer of transverse fiber bundles (90°) at a distance of 5 mm from each other. G-WEAVE™ is a woven fabric with large tows of approximately 4 mm, and with the same areal mass in both warp and weft directions (Fig. 2a and b). The two fabrics have the same sizing, compatible with thermoplastic matrices. Properties of the two glass fabrics are reported in Table 1.

3.2. Test fluids for permeability measurement

In order to span a wide range of capillary numbers, model fluids with different viscosities and surface tensions have been used for flow experiments: two silicon oils 47V1000 and 47V12500 (BlueStar Silicones®) and aqueous solutions of poly(ethylene glycol) (PEG) (M_w = 35 kDa, Sigma Aldrich) at various concentrations, containing a small amount of food colorant for contrast enhancement. Fluid types and corresponding physical properties are listed in Table 2. Viscosities were measured in continuous shear mode in a concentric cylinder rheometer (AR2000ex, TA Instrument), by means of a Peltier couette setup. Temperature ramps were performed from 15 °C to 25 °C at 0.1 °C/min at a constant shear-rate of either 1 s^{-1} or 10 s^{-1}. Viscosity-temperature behavior is fitted with an Arrhenius relation

$$\eta(T) = A\exp\left[-\frac{E_a}{RT}\right]. \quad (12)$$

The constants A and E_a were determined for each fluid.

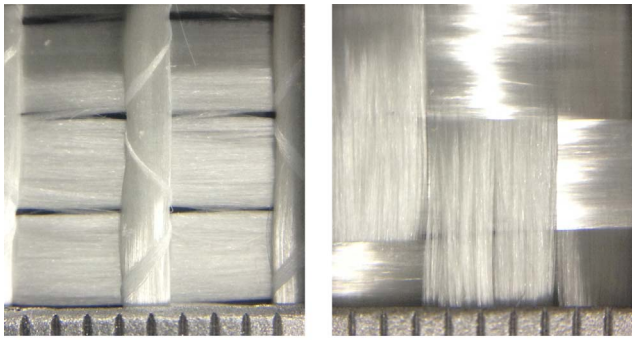

Fig. 2. (a) G-PLY and (b) G-WEAVE glass fabrics (unit length: 1 mm).

Table 1
Properties of glass fabrics (Chomarat™).

Fabric	Areal weight (0°)	Areal weight (90°)	Stitches density	Fiber radius	Glass density
–	(g/m^2)	(g/m^2)	(g/m^2)	(μm)	(g/cm^3)
G-PLY™	240	480	5	7.6 ± 0.9	2.62
G-WEAVE™	300	300	–	7.6 ± 0.9	2.62

Table 2
Properties of test fluids used for permeability measurements.

Fluid	Viscosity (20 °C)	E_a	A	Density	Surface tension
	Pa s	kJ K^{-1} mol^{-1}	Pa s	g/ml	mN/m
Water/colorant	0.00125	−12.41	$7.679{\cdot}10^{-6}$	0.997[a]	68.9
PEG 2%	0.00280	−18.73	$1.292{\cdot}10^{-6}$	1.001[a]	59.9
PEG 16.7%	0.111	−20.67	$2.312{\cdot}10^{-5}$	1.026[a]	57.3
PEG 30%	0.841	−21.41	$1.290{\cdot}10^{-4}$	1.050[a]	56.6
BlueSil 47V1000	1.13	−13.29	$4.835{\cdot}10^{-3}$	0.970[a]	21.1[a]
BlueSil 47V12500	13.6	−13.26	$5.876{\cdot}10^{-2}$	0.973[a]	21.1[a]

[a] Values at 25 °C.

Surface tension in air was measured at ambient temperature by the pendant drop method using a Drop Shape Analyzer (DSA30, Krüss). Density of PEG solutions was found in literature [33]. For silicon oils, the values provided by the supplier were used. Density and surface tension values were considered constant within the temperature range of tests, as they vary more slowly with temperature than viscosity.

3.3. Permeability measurements

Flow experiments for permeability measurement have been carried out on G-PLY and G-WEAVE in the setup shown in Fig. 3, which mainly comprises a rigid mold with a transparent glass top and an injecting unit. A single experiment allows simultaneous measurement of both unsaturated and saturated permeabilities, which are measured from the velocity of the fluid during fabric impregnation (transient state) and after the fabric is fully impregnated (steady state), respectively.

Fabric layers were accurately hand-cut with a width of 4.95 ± 0.05 cm and a length of 25 cm (G-PLY) or 23 cm (G-WEAVE), in order to fit in the mold cavity for permeability measurements and to prevent the occurrence of any race-tracking or channeling. For each experiment, the fabric mass was measured for accurate fiber volume fraction determination. For both fabrics, layers were laid all with the

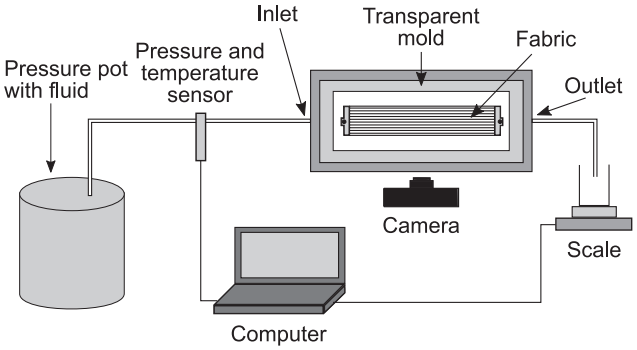

Fig. 3. Setup for permeability measurement at constant applied pressure.

Table 3
Fabric samples configurations.

Fabric	Layers	V_f (%)
G-PLY	4	36.47 ± 0.14
G-PLY	5	45.78 ± 0.40
G-PLY	6	55.24 ± 0.27
G-WEAVE	5	38.00 ± 0.08
G-WEAVE	6	45.07 ± 0.12
G-WEAVE	8	60.72 ± 0.19

same lay-up. Three different volume fractions were tested for each fabric type, by varying the number of layers, 4-, 5- and 6-layers for G-PLY, and 5-, 6- and 8-layers for G-WEAVE (Table 3). The fabric stack height was kept constant for all the experiments, by compacting it within a metallic frame of thickness 3.04 mm. A silicone joint between the frame and the fabric prevented fluid leakage and minimized race-tracking. The fluid was injected into the mold cavity from a pressure pot constantly supplied with compressed air, which guarantees a constant pressure to be applied on the fluid reservoir. The actual relative fluid pressure and temperature were measured right before the inlet with a sensor Keller Series 35XHTT. The advancement of the flow front was recorded through the glass top with digital camera Canon EOS700D. Lines were drawn equally spaced of 1 cm on the glass transversely to the flow direction. The video was subsequently analyzed so as to construct a plot of flow front position versus time by reporting the time at which the flow front reached each line. Outcoming fluid was collected in a beaker and continuously weighed with a scale. Mass flow was converted into flow rate by dividing by the fluid density for saturated permeability determination.

Unsaturated permeability was calculated from experimental data according to the squared flow front (SFF) method [21], which is recommended for unidirectional, in-plane flow under constant applied pressure, as

$$K_{SFF} = -\frac{m(1-V_f)\eta}{2\Delta P} \tag{13}$$

where m is the slope of the linear plot of the square of flow front position as a function of time. The data for the analysis was taken from the last part of the unsaturated flow, when the pressure is stabilized, typically starting from an impregnated length of 13 cm, as shown from the example in Fig. 4. The pressure was taken as the average value in this range. Capillary number was calculated from Eq. (1) using the flow-front velocity. Capillary number is not constant, because in a constant-pressure impregnation fluid velocity decreases as the flow-front advances from inlet to outlet. In order to assign a single Ca value to each experiment, the average flow-front velocity in the range of analysis was used, and a confidence interval was estimated from the standard deviation.

The saturated permeability was calculated from the flow rate of the fluid at the outlet, Q_{out}, using the following relation

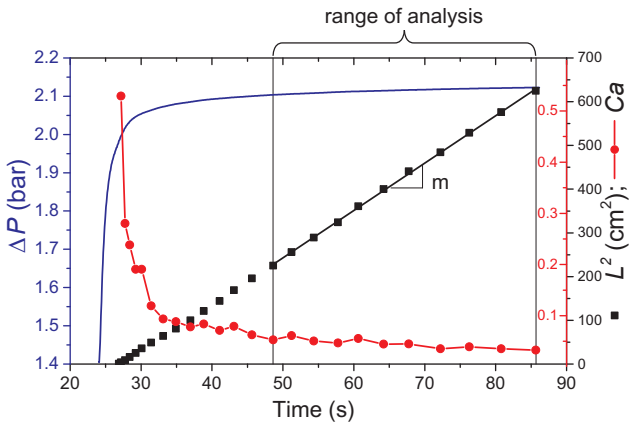

Fig. 4. Example of squared flow front, pressure and capillary number evolution with time for an experiment, showing the range of analysis. (For interpretation of the references to colour in this figure legend, the reader is referred to the web version of this article.)

$$K_{sat} = -\frac{Q_{out}\eta L_f}{A\Delta P} \tag{14}$$

where A is the cross-section area of the fabric stack, L_f is its length and ΔP is the average pressure during saturated flow. For each test, the fluid viscosity was calculated from the Arrhenius law (Eq. (12)) using the average experimental temperature. At least four experiments were carried out for each type of sample listed in Table 3, which allowed estimation of error bars from the standard deviation. Finally, for each experiment the ratio between unsaturated and saturated permeability was simply calculated as

$$R_s = \frac{K_{SFF}}{K_{sat}}. \tag{15}$$

3.4. Fabrics microstructural characterization

Microstructures of the two fabric types were characterized using a laboratory X-ray microtomograph (RX Solutions, PIXE Platform, EPFL, Switzerland). Samples were inserted into cylindrical PMMA containers and compacted to the thickness of 3 mm as detailed in [34]. Six fabric samples were analyzed, reproducing the same configurations as in the permeability experiments (Table 3). During the measurements, the generator voltage and the current intensity were set to 160 kV and 200 μA and 2000 radiographs were acquired with the size of 2176 × 1792 pixels from the incremental rotation of the samples with respect to the X-ray source. In a following reconstruction operation, 3D grayscale images of absorption coefficients were obtained with a voxel size of 9.87 × 9.87 × 9.87 μm^3.

3.4.1. Image analysis

The tomographic reconstructions for the six samples, with a size of 1475 × 1475 × 304 voxels, are shown in Fig. 5. In order to investigate the channel structure of scanned G-PLY samples, 3D images were converted to 2D slices along the x-direction (i.e., each slice was on the yz-plane) and each 2D slice was segmented to consist of fiber bundles and meso-channels. Segmentation was achieved using Fiji [35], and a standard thresholding procedure was followed by additional morphological operations. Fig. 6 illustrates 2D slices and their corresponding binary images; meso-channels of the samples showed distinct characteristics in terms of their cross-sectional geometries. Channels in 4-layer and 6-layer samples exhibited rectangular and triangular shapes, respectively; whereas the 5-layer sample contained both rectangular and triangular meso-channels. Even though the nesting and layer shifting mechanisms are beyond the scope of this study, it is obvious that increasing the number of layers caused shrinkage of the rectangular channels combined with bending of the bundles in the transversal

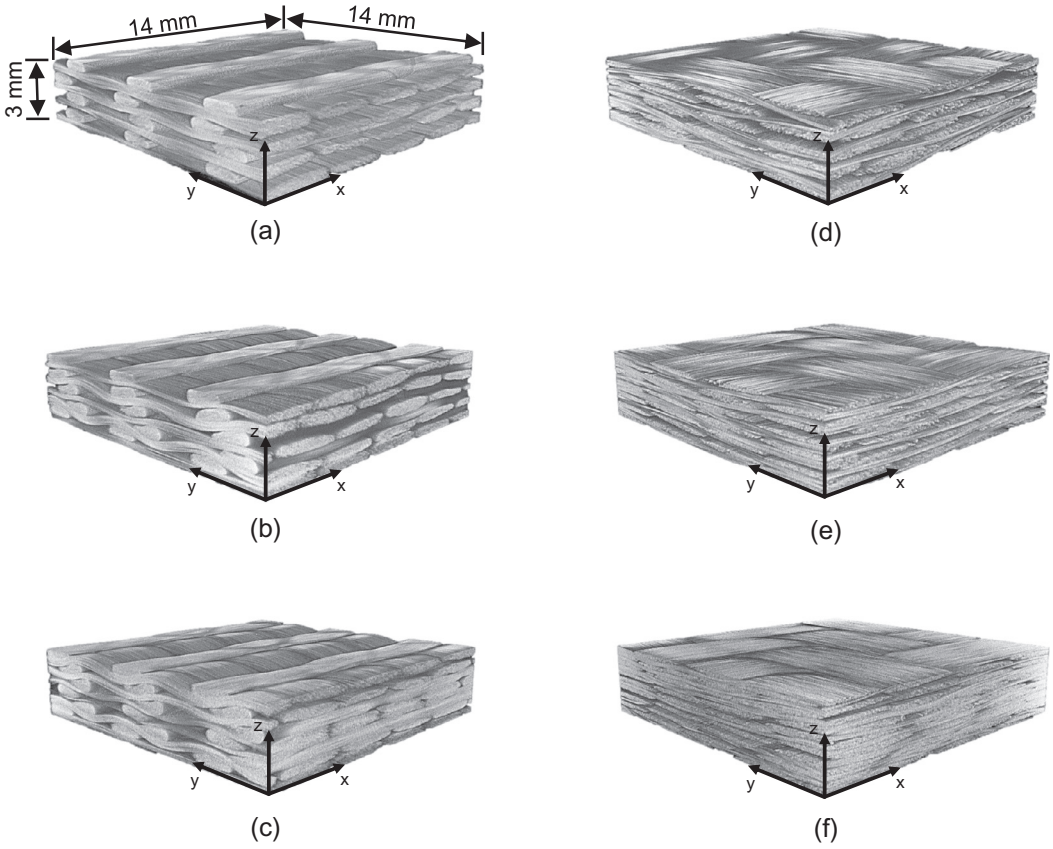

Fig. 5. 3D images reconstructed from computer X-ray tomography of G-PLY with (a) 4, (b) 5 and (c) 6 layers and G-WEAVE with (d) 5, (e) 6 and (f) 8 layers.

direction, which in turn resulted in the formation of smaller triangular channels. For the 5-layer sample, intermediate compaction results in hybrid channels' shape, with both triangular and rectangular channels forming at different locations along the longitudinal direction. To quantify the channel geometry, Analyze Particles plugin of Fiji was used in all 2D slices except those corresponding to the interbundle gaps between the adjacent transversal bundles. In addition to the area and perimeter of the pores, the aspect ratio of each pore's bounding box was also measured and used as a shape descriptor to distinguish between rectangular and triangular pore geometries as will be detailed in Section 4.2.2.

4. Results and discussion

4.1. Saturated permeability

Fig. 7 displays the measured values of saturated permeability for the six fabric configurations. The permeability of G-PLY is almost one order of magnitude higher than that of G-WEAVE for comparable fiber content, and is also higher than that of typical glass fabrics, which makes it

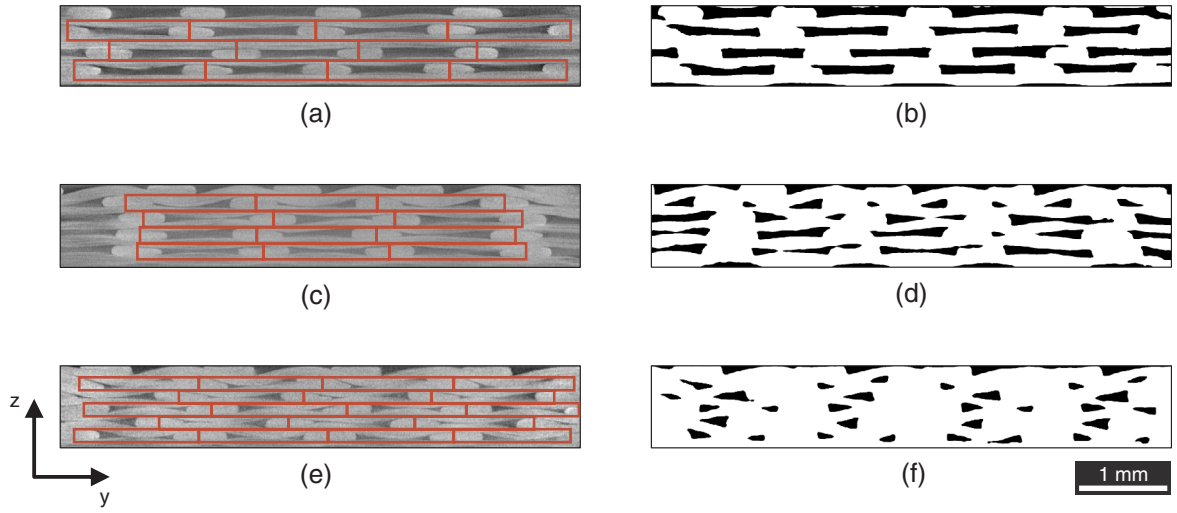

Fig. 6. Cross section views from computed X-ray tomography showing unit cells (left-hand side) and binary-converted images showing varying meso-channel shapes (right-hand side) for (a-b) 4, (c-d) 5 and (e-f) 6 layers of G-PLY; respectively 11, 12 and 18 unit-cells were used for image analysis of the three samples, each containing either one rectangular or two parallel triangular meso-channels. (For interpretation of the references to colour in this figure legend, the reader is referred to the web version of this article.)

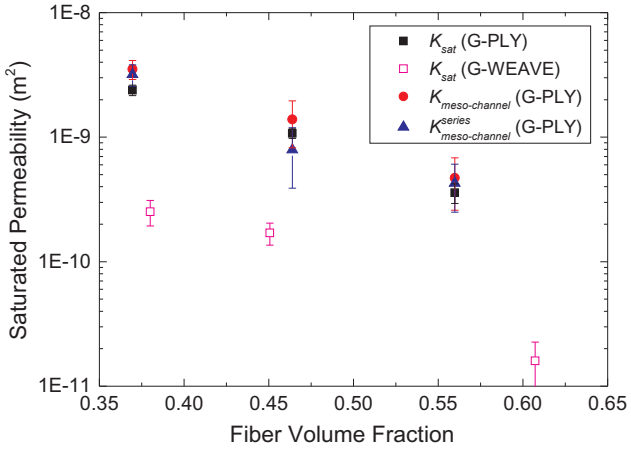

Fig. 7. Saturated permeability for G-PLY and G-WEAVE glass fabrics, along with numerical values obtained from meso-channel geometry analysis. (For interpretation of the references to colour in this figure legend, the reader is referred to the web version of this article.)

suitable for fast impregnation with highly viscous resins. This is attributed to the different meso-structures of the two fabrics, as the characteristics at micro-scale (e.g. sizing and fiber radius) are the same.

4.2. Microstructural analysis

4.2.1. Meso-channel geometry

In order to analyze the channel cross-section throughout the whole sample, 3D binary subvolumes were cropped to contain individual meso-channels. This operation resulted in 11, 12 and 18 3D subvolumes for 4, 5, and 6-layer samples, respectively (see Fig. 6). Each 3D subvolume consists of 2086 slices, from which we analyzed on average 1459 ± 199 rectangular cross-sections for 4-layer sample, 687 ± 124 rectangular and 1332 ± 214 triangular cross-sections for 5-layer sample, and 2651 ± 385 triangular cross-sections for 6-layer sample. Fig. 8a, c and e show the aspect ratio and the area of the detected cross-sections in each slice of the samples as well as typical channel geometries and their bounding boxes. A comparison between the channel characteristics of different samples indicates that rectangular channels typically cover a larger area than the triangular channels and their bounding boxes have larger aspect ratios. Both channel types are present in 5-layer sample and results in two clusters in terms of aspect ratio and area as observed in Fig. 8. This confirms that, in the 5-layer sample, the channels are locally constricted due to local compaction and bending of bundles, thus a rectangular channel splits into two smaller triangular channels, which later on converge back to form a single rectangular channel.

4.2.2. Estimation of permeability from meso-channels geometry

Using a circuit analogy, the pressure drop in a channel is related to the flow rate as

$$-\Delta P = R_{hyd} Q_{out} \tag{16}$$

where R_{hyd} is the hydraulic resistance. Even though expressions for hydraulic resistance of ideal cross-sections (i.e., circle, ellipse, rectangle, etc.) can be found, channels encountered herein are far from ideal. Thus, R_{hyd} of each channel was calculated using the general expression as proposed by Bruus [36]:

$$R_{hyd} = \frac{2\eta L_c P_c^2}{A_c^3} \tag{17}$$

where P_c and A_c are respectively the perimeter and area of the channel cross-section, and L_c is the channel length. The characteristic R_{hyd} of each channel in Fig. 6 was estimated using the median perimeter and median area measurements obtained using the Analyze Particles plugin. Combining Eqs. (14), (16) and (17), permeability of the 4-layer and 6-layer samples are then calculated as

$$K_{meso-channel} = \frac{A_c^3}{2P_c^2 A} \tag{18}$$

where A is the cross-sectional area of the unit cell (red boxes in Fig. 6) along the flow direction with width of 5 mm corresponding to the center-to-center distance between two adjacent tows in a layer and the height of 0.75 and 0.5 mm calculated as $3/n$ (mm), n being the number of layers. In the 5-layer sample, two triangular channels are considered as two resistances in parallel, in series with another resistance corresponding to the rectangular channel (see Fig. 9). To calculate the R_{hyd} of each channel type, channels are clustered into two groups using the area and aspect ratio of the bounding box in k-medoids function of Matlab (see Fig. 8a, c and e for clusters) using the median perimeter and median area values of each cluster. Once the permeabilities of triangular and rectangular channels ($K_{meso,t}$,$K_{meso,r}$) are calculated using Eq. (18), permeability of a full meso-channel is then calculated as

$$K_{meso-channel} = \frac{l_r + l_t}{\frac{l_r}{K_{meso,r}} + \frac{l_t}{K_{meso,t}}} \tag{19}$$

where l_r and l_t are the relative lengths of rectangular and triangular channels, calculated by using the number of elements in each respective cluster. It should be noted that A in Eq. (18) is the cross-sectional area of the unit cell with the width of 5 mm and the height of 0.6 mm. Permeability results are presented in Table 4 along with the characteristics of the channel cross-sections. A comparison between the experimental and meso-channel based permeability values (Fig. 7) shows that this model, despite its simplicity, results in a reasonably close estimation of permeability, within the same order of magnitude as experimental results. Eq. (17) overestimates the permeability of rectangular channels if the aspect ratio is higher than 2.27, obtained by solving Eq. (17) and the expression for R_{hyd} of rectangular cross-section $\left(R_{hyd} = \frac{12\eta L_c}{1 - 0.63\frac{h}{w}} \frac{1}{h^2 w}\right)$; aspect ratios of rectangular cross-sections are significantly higher than this critical value in both 4- and 5-layer samples (see Fig. 8). The overestimation due to this formulation is 32.3% for an aspect ratio of 1:10, a typical value of aspect ratio as seen in Fig. 8a. In addition, triangular channels are assumed to be all identical in the model and this can contribute to an overestimation of permeability. However, identification of individual channels is not straightforward and requires a pore network analysis, which is beyond the scope of this work.

An alternate approach consists in considering a channel whose cross-section varies along the length as N infinitesimally short ducts connected in series. A permeability value K_i is then calculated for the cross-sections in any of the i-th slice from Eq. (18), the distribution of which along a single meso-channel is displayed in the histograms of Fig. 8b, d and f. Thus, the permeability of each channel, be it rectangular or triangular, is calculated as

$$K^{series}_{meso-channel} = \frac{N}{\sum_{i=1}^{N} \frac{1}{K_i}}. \tag{20}$$

In the case of 4 and 6-layers samples, where either rectangular or triangular channels are present, Eq. (20) is used straightforwardly. For 5-layers sample, a meso-channel is again considered as two rectangular channels connected in series with a pair of parallel triangular channels (Fig. 9b). First, permeability of the triangular portion is calculated, considering that any i-th slice contains two triangular cross-sections of area $A_i^{(1)}$ and $A_i^{(2)}$. The equivalent permeability of each slice is then calculated as the weighted average of the two triangles:

$$K_i = c_i^{(1)} K_i^{(1)} + c_i^{(2)} K_i^{(2)}, \tag{21}$$

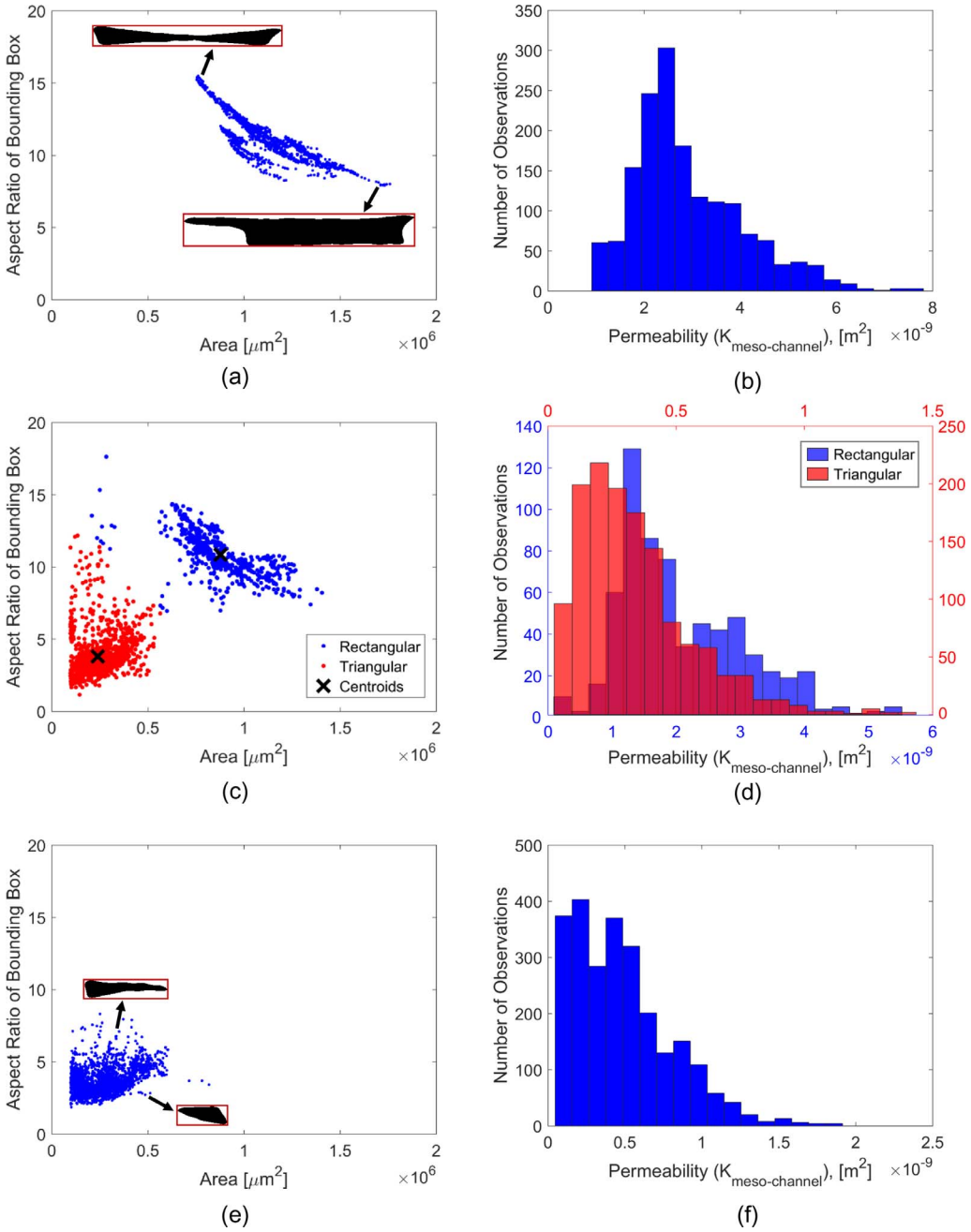

Fig. 8. Aspect ratio and area (left-hand side) and permeability based on Eq. (18) (right-hand side) of cross-sections along a single channel for (a-b) 4, (c-d) 5 and (e-f) 6 layers samples. (For interpretation of the references to colour in this figure legend, the reader is referred to the web version of this article.)

where we defined the relative cross-sectional areas of the i-th slice as:

$$c_i^{(1)} = \frac{A_i^{(1)}}{A_i^{(1)} + A_i^{(2)}}$$

$$c_i^{(2)} = \frac{A_i^{(2)}}{A_i^{(1)} + A_i^{(2)}},$$

and $K_i^{(1)}$ and $K_i^{(2)}$ are the permeabilities of the two triangular cross-sections in the i-th slice which are again obtained from Eq. (18). Eq. (20) is then used to calculate the permeability of the whole meso-channel, where K_i are taken from Eq. (18) for the rectangular portions and Eq. (21) for the triangular portion. Finally, once the permeability is calculated for all the channels shown in Fig. 6a, c and e, the average permeability of these parallel channels is calculated. The values are reported in Table 4 and displayed in Fig. 7. Ultimately, it can be concluded that both approaches lead to values which are coherent with the experimental results.

4.2.3. Equivalent permeability of the unit cell

Circuit analogy for estimation of equivalent resistance in channels is valid for low Reynolds numbers and, in case of non-crimp biaxial fabrics, can be extended to calculate the equivalent permeability of the unit cell by taking into account the three distinct flow zones as shown in Fig. 10:

- flow through the meso-channel, with permeability $K_{meso}^{\parallel}$,
- flow through fiber bundles along the flow, with permeability $K_{micro}^{\parallel}$,
- flow through the transverse bundles with permeability $K^{\perp}$, which is broken down to two components:
  - flow through fiber bundles perpendicular to flow ($K_{micro}^{\perp}$),

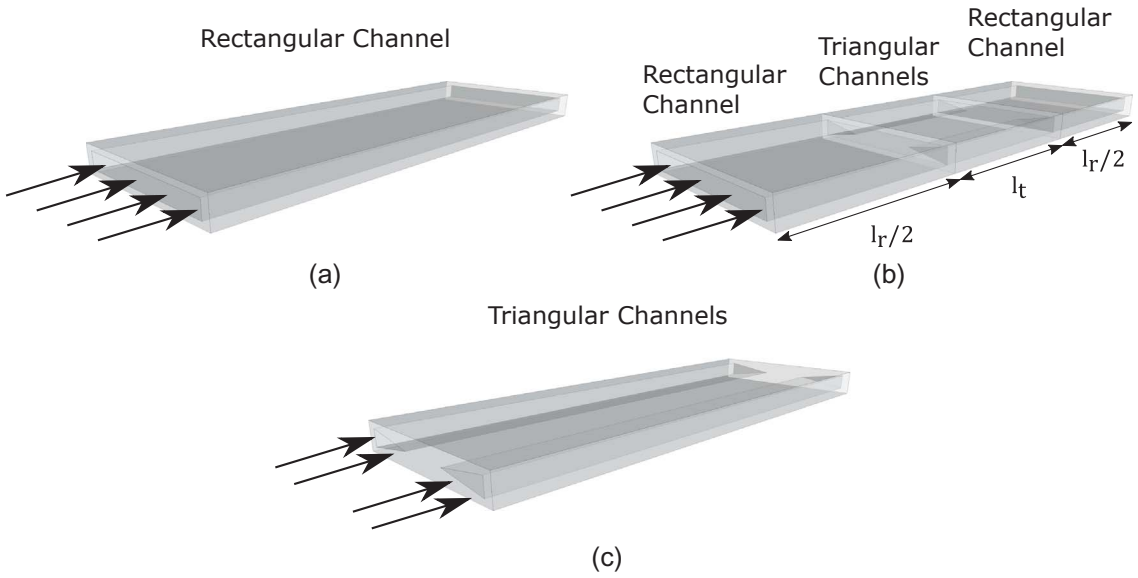

Fig. 9. Scheme of (a) rectangular channel, (b) rectangular and triangular channels in series, and (c) triangular channels in parallel.

Table 4
Geometrical parameter and permeability of the meso-channels for the 4, 5 and 6-layers samples. Experimental saturated permeability is also reported.

	$A_{c,r}$ (10^5 μm^2)	$P_{c,r}$ (10^3 μm)	$A_{c,t}$ (10^5 μm^2)	$P_{c,t}$ (10^3 μm)	l_r (μm)	l_t (μm)	$K_{meso-channel}$ (m^2)	$K^{series}_{meso-channel}$ (m^2)	K_{sat} (m^2)
4 layers	10.25 ± 0.76	8.18 ± 0.33	0	0	1	0	$(3.52 \pm 0.61)\cdot10^{-9}$	$(3.19 \pm 0.62)\cdot10^{-9}$	$(2.39 \pm 0.23)\cdot10^{-9}$
5 layers	9.041 ± 0.931	7.77 ± 0.49	3.045 ± 0.624	3.08 ± 0.34	0.516 ± 0.119	0.484 ± 0.119	$(1.39 \pm 0.57)\cdot10^{-9}$	$(7.91 \pm 4.02)\cdot10^{-10}$	$(1.074 \pm 0.096)\cdot10^{-9}$
6 layers	0	0	2.490 ± 0.616	2.59 ± 0.39	0	1	$(4.71 \pm 2.12)\cdot10^{-10}$	$(4.28 \pm 1.78)\cdot10^{-10}$	$(3.58 \pm 0.64)\cdot10^{-10}$

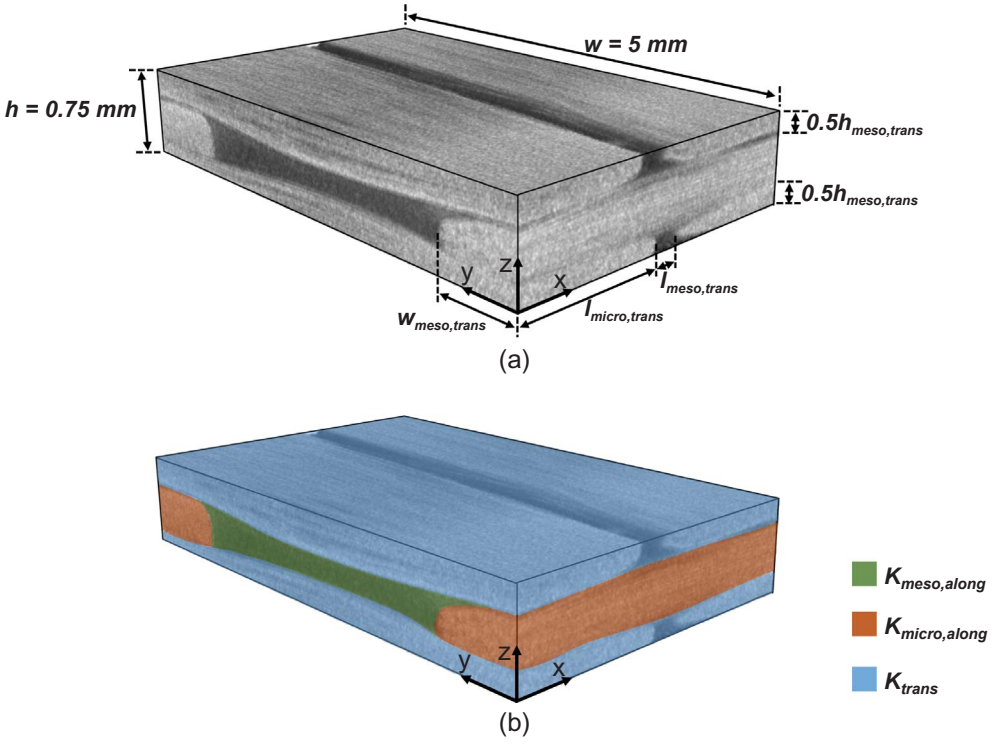

Fig. 10. Example of unit cell of G-PLY, showing (a) geometrical parameters and (b) the three flow zones. (For interpretation of the references to colour in this figure legend, the reader is referred to the web version of this article.)

Table 5
Equivalent permeability calculations.

	$K^{\parallel}_{meso}$ (m^2)	$V^{\parallel}_{f,micro}$	$K^{\parallel}_{micro}$ (m^2)	$V^{\perp}_{f,micro}$	$K^{\perp}_{micro}$ (m^2)	$h^{\perp}_{meso}$ (m)	$K^{\perp}_{meso}$ (m^2)	$l^{\perp}_{meso}$	$l^{\perp}_{micro}$	$K^{\perp}$ (m^2)	c_1	c_2	c_3	K_{eq} (m^2)
4 layers	$(1.08 \pm 0.13)\cdot10^{-8}$	0.644	$9.33\cdot10^{-13}$	0.375	$4.92\cdot10^{-11}$	$(4.65 \pm 0.73)\cdot10^{-4}$	$1.70\cdot10^{-8}$	0.104 ± 0.0436	0.896 ± 0.0436	$5.48\cdot10^{-11}$	0.321	0.190	0.489	$3.53\cdot10^{-9}$
5 layers	$(5.23 \pm 1.31)\cdot10^{-9}$	0.675	$6.44\cdot10^{-13}$	0.425	$3.81\cdot10^{-11}$	$(4.25 \pm 0.69)\cdot10^{-4}$	$1.42\cdot10^{-8}$	0.0842 ± 0.0539	0.9158 ± 0.0539	$4.16\cdot10^{-11}$	0.242	0.226	0.532	$1.29\cdot10^{-9}$
6 layers	$(2.28 \pm 0.43)\cdot10^{-9}$	0.689	$5.47\cdot10^{-13}$	0.458	$3.26\cdot10^{-11}$	$(3.63 \pm 0.86)\cdot10^{-4}$	$1.05\cdot10^{-8}$	0.0595 ± 0.0481	0.9405 ± 0.0481	$3.47\cdot10^{-11}$	0.204	0.266	0.530	$4.83\cdot10^{-10}$

– flow through the meso-channel between two adjacent fiber bundles perpendicular to the flow ($K^{\perp}_{meso}$) [37–39].

$K^{\parallel}_{meso}$ was calculated using the methodology detailed in the previous section except that this time, it was based on the cross-sectional area (A_c) of the channel itself, instead of that of the unit cell (red boxes in Fig. 6), reducing Eq. (18) to the following:

$$K^{\parallel}_{meso} = \frac{A_c^2}{2P_c^2}. \tag{22}$$

In order to calculate the permeability within the bundles parallel and perpendicular to the flow, the volume fraction of bundles ($V^{\parallel}_{f,micro}$ and $V^{\perp}_{f,micro}$) were calculated by manually fitting splines to at least 40 individual bundle cross-sections in each direction. Using the TEX value (1200 for both warp and weft bundles) and fiber radius, the values of volume fractions reported in Table 5 were calculated. Permeability of the bundles along and transverse to flow direction were calculated using Gebart's equations, i.e. respectively

$$K^{\parallel}_{micro} = \frac{8}{C_1}\frac{(1-V^{\parallel}_{f,micro})^3}{(V^{\parallel}_{f,micro})^2}R^2 \tag{23}$$

and

$$K^{\perp}_{micro} = C_2\left(\sqrt{\frac{V_{f,max}}{V^{\perp}_{f,micro}}}-1\right)^{5/2}R^2 \tag{24}$$

where $C_1 = 53$, $C_2 = \frac{16}{9\pi\sqrt{6}}$ and $V_{f,max} = \frac{\pi}{2\sqrt{3}}$ for hexagonal fiber arrangement [40], and $R = 7.55 \pm 0.89$ μm is the average fiber radius. The meso-channel between the two transverse bundles, whose permeability is denoted by $K^{\perp}_{meso}$, is assumed to have a rectangular cross-sectional area with a width of 5 mm (spacing between the centers of two bundles along the flow) and with height equal to the height of transverse bundles ($h^{\perp}_{meso}$). Permeability of this rectangular channel is calculated as

$$K^{\perp}_{meso} = \frac{\left(1-0.63\frac{h}{w}\right)h^2}{12} \tag{25}$$

where h and w are height and width of the unit cell, respectively. The equivalent transverse permeability ($K^{\perp}$) is calculated by considering the meso- and micro-flow and is calculated as

$$K^{\perp} = \frac{l^{\perp}_{meso} + l^{\perp}_{micro}}{\frac{l^{\perp}_{meso}}{K^{\perp}_{meso}} + \frac{l^{\perp}_{micro}}{K^{\perp}_{micro}}} \tag{26}$$

since the two channels are treated as two resistances connected in series (see Fig. 10a). As shown in Fig. 10b, the three flow zones in the unit cell, namely flow in the parallel bundles (orange), flow in the meso-channel (green) and the transverse flow (blue) take place in parallel. Using the relative cross-sectional area of each of the three zones in the unit cell (c_1, c_2, and c_3, see Table 5), the overall equivalent permeability is thus:

$$K_{eq} = c_1K^{\parallel}_{meso} + c_2K^{\parallel}_{micro} + c_3K^{\perp}. \tag{27}$$

Values are reported in Table 5. A comparison between K_{eq} and $K_{meso-channel}$ calculated in the previous section show that the results are very close (less than 8% deviation) for all of the three samples, validating the approach presented in the previous section which considers only flow in the meso-channels.

4.3. Unsaturated permeability

The differences in architecture of the two fabric types influence the unsaturated flow morphology for different capillary numbers, as illustrated in Fig. 11. The G-WEAVE shows a "classic" behavior, with a narrow unsaturated zone confined at the flow front for both low

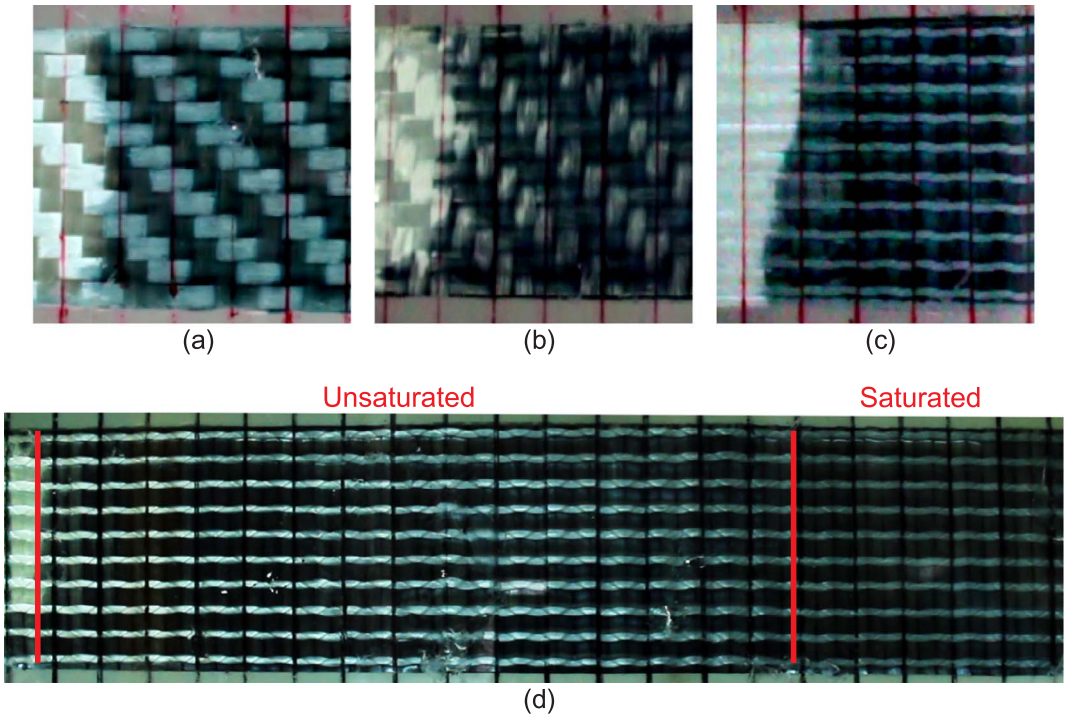

Fig. 11. Flow front at capillary number 0.000068 (a) and 0.0028 (b) for G-WEAVE and 0.00013 (c) and 0.38 (d) for G-PLY. (For interpretation of the references to colour in this figure legend, the reader is referred to the web version of this article.)

(Fig. 11a) and high (Fig. 11b) *Ca* values. At low *Ca*, flow is slightly faster in the intra-tow region, because driven by capillarity, resulting in no visible dry regions in the saturated zone behind the flow front (Fig. 11a), whereas at higher *Ca* flow is dominant in the inter-tow spaces, causing entrapment of dry spots in the fiber bundles (Fig. 11b). Conversely, in the G-PLY, flow is never dominant in the fiber bundles. At low *Ca* the flow front morphology remains rather close to "slug-flow", showing no leading flow in the bundles (Fig. 11c), whereas at higher *Ca*, the fluid clearly flows faster in the meso-channels than in the bundles, leaving behind a large unsaturated area (Fig. 11d).

Varying the applied pressure, fluid type and fiber volume fraction, it was possible to perform experiments in a range of average capillary numbers spanning over four orders of magnitude. Due to its particular structure with large channels, which confers to G-PLY such a high permeability, this fabric was able to allow flow of high viscosity fluids (>10 Pa s) at relatively low pressure (<5 bar) and without destruction or visible deformation of the preform architecture, allowing to reach capillary numbers as high as 0.4. In G-WEAVE, *Ca* could not exceed ~ 0.04; beyond this value fabric deformation was observed. For each experiment, the ratio between unsaturated and saturated permeability defined in Eq. (15) was reported as a function of capillary number; overall results are given in Fig. 12a, where each point corresponds to a single experiment. The error bars on the x-axis correspond to the standard deviation for the capillary number in the range of analysis of each test (Fig. 4). The large scatter of data points is attributed to variations of capillary number and to experimental variability in permeability measurements, which is largely documented for this kind of tests [20]. Nonetheless, trends are observed: at small capillary numbers, R_s is higher than 1 for all experiments, and decreases rapidly as *Ca* increases. For $0.0005 \lesssim Ca \lesssim 0.01$, values smaller than 1 are mainly observed for G-WEAVE. Finally, for higher *Ca*, R_s increases again to around 1 or above. This behavior results from the competition between capillary phenomena within the fiber bundles (intra-tow) and viscous flow in the gaps between the bundles (inter-tow). When *Ca* is low, fluid is driven in the narrow intra-tow spaces by capillary forces, leading (in accordance with Eq. (15)) to an overestimation of the unsaturated permeability compared to the saturated value. This is particularly true for the G-WEAVE, for which the highest R_s values were observed at $Ca < 0.0005$. Above a critical *Ca*, viscous flow starts to dominate, and R_s is expected to drop below 1, as the fluid flows preferentially in between the tows. This transition from wetting to non-wetting flow as *Ca* increases was observed in non-crimp carbon fabrics in [13], and is confirmed in this study for the G-WEAVE, for capillary number values between $5{\cdot}10^{-4}$ and $1{\cdot}10^{-2}$. However, for G-PLY, R_s remained close to 1 in most of the experiments at higher capillary numbers. However, this cannot be attributed to capillary effects, as flow mostly takes place in the inter-tow spaces (meso-channels), delaying impregnation of the fiber bundles. When the inter-tow spacing is large, saturated permeability was shown above to be well predicted by a flow channel model neglecting any flow in the fiber tows. As a result, the flow kinetics measured for G-PLY are dominated by flow in the meso-channels, and do not differ much from those observed close to the critical capillary number, for which flow takes place equally in both tows and channels.

Following Eq. (11), capillary pressure can be estimated as

$$\Delta P_\gamma = \Delta P(R_s - 1). \tag{28}$$

The results are plotted in Fig. 12b. For the G-WEAVE, $\Delta P_\gamma < 0$ at low *Ca* and mainly $\Delta P_\gamma > 0$ at high *Ca*, confirming the transition from wetting to non-wetting at $Ca^* \sim 0.0005$. For G-PLY, $\Delta P_\gamma \sim 0$ at mid-low *Ca*, i.e. capillary effects are negligible. For higher *Ca*, the negative capillary pressure values are to be considered as an apparent pressure (apparent wetting). This rises from the fact that for this fabric and at high *Ca* the flow is definitely far from the slug-flow assumption, and Eq. (28) is no longer valid.

The critical capillary number corresponding to a transition from wetting to non-wetting (Ca^*) has been discussed by previous authors [10,13–17] in view of process optimization, as it corresponds to a minimum void content. As a result, it is often referred to as optimum capillary number. At this value, capillary and hydrodynamic forces compensate and fluid flows at the same velocity in the inter- and intra-tow regions, leading to a minimum amount of entrapped voids in the final composite. Values between 10^{-3} and 10^{-2} have been reported by these authors. In the present study, a lower value (approximately 0.0005) is observed. This is not surprising, as the optimal capillary

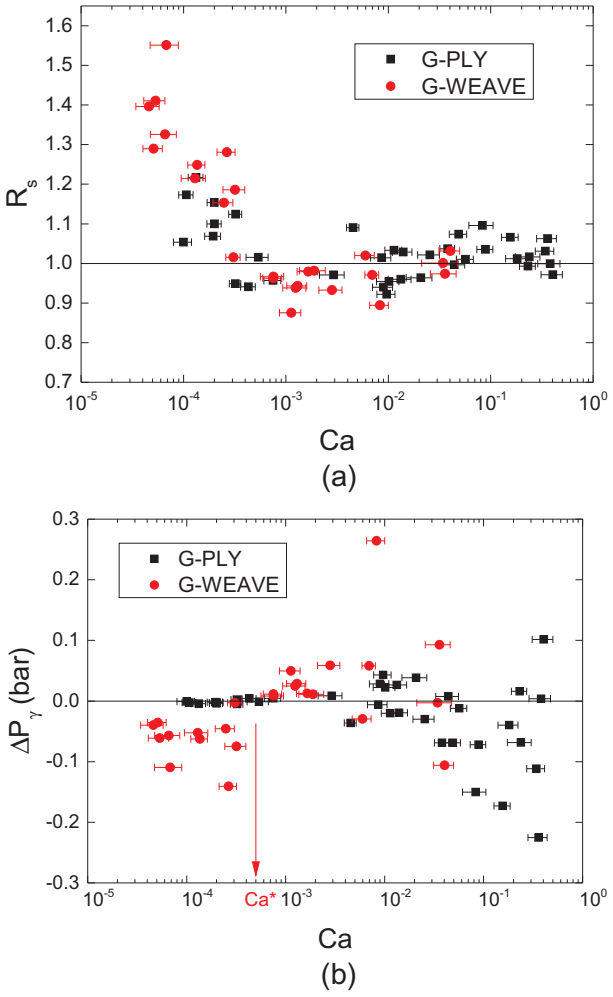

Fig. 12. (a) Unsaturated-to-saturated permeability ratio and (b) capillary pressure vs. average capillary number for the whole series of tests. (For interpretation of the references to colour in this figure legend, the reader is referred to the web version of this article.)

number is expected to vary with fabric architecture and type [10,17]. For instance, carbon fibers have smaller diameter and higher specific surface area, which is responsible for stronger capillary effects. Consequently, the value Ca^*, at which viscous forces overcome capillary forces, is expected to be higher (see for example [13,14]). It is also worthy to note that the standard deviation on capillary number in this study lies between 15 and 25%, as it was estimated in established flow regions under constant applied pressure. In order to find a more precise optimum capillary number, constant flow rate experiments should be performed [13,14]. However, these are more difficult to perform, both in terms of experimental practicality (constant-flow-rate injecting system is needed, like a pump or syringe) and of data analysis (optimal capillary number is determined from capillary pressure drop taken as the y-intercept of the inlet-pressure build-up graph, which is dramatically affected by the chosen range of analysis). On the contrary, the experimental methodology hereby proposed would allow to determine the optimal capillary number for a given fabric by a small series of constant-pressure tests performed at different capillary numbers by simply comparing unsaturated and saturated permeabilities. Nonetheless, following this methodology, it should be possible in a future study to determine the optimal *Ca* value by comparing saturated and unsaturated permeabilities through a relatively small number of experiments.

5. Conclusion

Unsaturated and saturated permeability were measured and estimated for a non-crimp fabric (G-PLY) whose peculiar channel-wise structure allows for fast impregnation with high-viscosity resins, and for a regular woven fabric (G-WEAVE). Saturated permeability was found to be one order of magnitude greater for the G-PLY fabric, which is key for the development of a resin transfer molding process with melt thermoplastic resins [25]. It is however important to note that the flow front is, in many cases with this fabric, not uniform; care must be taken to ensure full impregnation of the tows in processing composites with these materials. We demonstrated that permeability for these fabrics is dominated by viscous flow along the meso-channels for a broad range of capillary numbers. As a result, a numerical model based on the hydraulic circuit analysis, which requires a rather basic knowledge of the flow channels' geometry provides good agreement with experimental results. Implementation of a model taking into account the micro-flow in the intra-tow pores confirms this trend, with only minor improvement on the permeability estimation.

The ratio of unsaturated over saturated permeability was also measured through constant-pressure experiments performed over a wide range of capillary numbers. This ratio can be theoretically estimated from the solution of Darcy's law taking into account or not the capillary pressure at the flow front; it is directly related to the ratio of capillary pressure over applied pressure. Experimental results confirmed that for a rather classic woven fabric (G-WEAVE), R_s is much greater than 1 at low capillary numbers, and decreases as flow velocity increases, to drop below 1 above a critical *Ca* value, which may represent the optimal *Ca* value as identified to ensure low porosity in LCM. For G-PLY, a similar behavior is initially observed, however R_s remains close to 1 for all capillary numbers above the critical value. This is attributed to the dominant effect of inter-tow flow in the overall flow kinetics. This work contributes to the long debate in the LCM community between unsaturated versus saturated flow measurement, to indicate that, in particular for fabrics which have a strong dual-scale nature, unsaturated permeability measurements can indeed provide an accurate measurement of permeability, as long as care is taken to perform the experiment at high enough *Ca* to favor inter-tow flow. *Ca* should however remain low enough to prevent fabric distortion during the experimental measurement. As a first practical application, determination of the range of capillary numbers from unsaturated permeability measurement only would thus require to perform a few experimental measurements at increasing pressure range, for example, and to select the values where the flow front is optically saturated, or with intra-tow flow leading, instead of those obtained when intra-tow flow is leading.

Acknowledgement

The authors acknowledge the Swiss Innovation Agency Innosuisse through the Swiss Competence Centre for Energy Research Efficient Technologies and Systems for Mobility (SCCER-Mobility), and Cytec/Solvay Group (Dr. G. Orange, Research Centre of Lyon, France) for funding this research, as well as Chomarat (Le Cheylard, France) for providing the glass fabrics. We also thank the SMaL laboratory at EPFL for use of their Drop Shape Analyzer.

References

[1] Zhu H, Wu B, Li D, Zhang D, Chen Y. Influence of voids on the tensile performance of carbon/epoxy fabric laminates. J Mater Sci Technol 2011;27(1):69–73. http://dx.doi.org/10.1016/S1005-0302(11)60028-5.

[2] Yun M, Carella T, Simacek P, Advani S. Stochastic modeling of through the thickness permeability variation in a fabric and its effect on void formation during Vacuum Assisted Resin Transfer Molding. Compos Sci Technol 2017;149:100–7. http://dx.doi.org/10.1016/j.compscitech.2017.06.016.

[3] Shih C-H, Lee LJ. Effect of fiber architecture on permeability in liquid composite

molding. Polym Compos 1998;19(5):626–39. http://dx.doi.org/10.1002/pc.10136.
[4] Pearce NRL, Summerscales J, Guild FJ. Improving the resin transfer moulding process for fabric-reinforced composites by modification of the fabric architecture. Compos Part A: Appl Sci Manuf 2000;31(12):1433–41. http://dx.doi.org/10.1016/S1359-835X(00)00140-8.
[5] Rieber G, Jiang J, Deter C, Chen N, Mitschang P. Influence of textile parameters on the in-plane Permeability. Compos Part A: Appl Sci Manuf 2013;52:89–98. http://dx.doi.org/10.1016/j.compositesa.2013.05.009.
[6] Cazaux G, Bizet L, Bréard J, Gomina M, Syerko E, Comas-Cardona S, et al. Permeability enhancement with different glass fiber quasi-UD structure arrangements for RTM-TP process. In: 20th International conference on composite materials, Copenhagen, Denmark; 2015.
[7] Martin B, Comas-Cardona S, Binetruy C, Billon N, Bouvard JL, Lucas P. Influence of fabrics' design parameters on the morphology and 3D permeability tensor of quasi-unidirectional non-crimp fabrics. Compos Part A: Appl Sci Manuf 2016;90:470–9. http://dx.doi.org/10.1016/j.compositesa.2016.08.013.
[8] Syerko E, Binetruy C, Comas-Cardona S, Leygue A. A numerical approach to design dual-scale porosity composite reinforcements with enhanced permeability. Mater Des 2017;131:307–22. http://dx.doi.org/10.1016/j.matdes.2017.06.035.
[9] Endruweit A, Zeng X, Matveev M, Long AC. Effect of yarn cross-sectional shape on resin flow through inter-yarn gaps in textile reinforcements. Compos Part A: Appl Sci Manuf 2018;104:139–50. http://dx.doi.org/10.1016/j.compositesa.2017.10.020.
[10] Patel N, Lee LJ. Effects of fiber mat architecture on void formation and removal in liquid composite molding. Polym Compos 1995;16(5):386–99. http://dx.doi.org/10.1002/pc.750160507.
[11] Patel N, Lee LJ. Modeling of void formation and removal in liquid composite molding. Part I: wettability analysis. Polym Compos 1996;17(1):96–103. http://dx.doi.org/10.1002/pc.10594.
[12] Binetruy C, Pabiot J, Hilaire B. The influence of fiber wetting in resin transfer molding: scale effects. Polym Compos 2000;21(4):548–57.
[13] Verrey J, Michaud V, Ma˚nson J-A. Dynamic capillary effects in liquid composite moulding with non-crimp fabrics. Compos Part A: Appl Sci Manuf 2006;37(1):92–102. http://dx.doi.org/10.1016/j.compositesa.2005.04.011.
[14] Zingraff L, Michaud V, Bourban P-E, Ma˚nson J-A. Resin transfer moulding of anionically polymerised polyamide 12. Compos Part A: Appl Sci Manuf 2005;36(12):1675–86. http://dx.doi.org/10.1016/j.compositesa.2005.03.023.
[15] Ruiz E, Achim V, Soukane S, Trochu F, Bréard J. Optimization of injection flow rate to minimize micro/macro-voids formation in resin transfer molded composites. Compos Sci Technol 2006;66(3-4):475–86. http://dx.doi.org/10.1016/j.compscitech.2005.06.013.
[16] Leclerc JS, Ruiz E. Porosity reduction using optimized flow velocity in Resin Transfer Molding. Compos Part A: Appl Sci Manuf 2008;39(12):1859–68. http://dx.doi.org/10.1016/j.compositesa.2008.09.008.
[17] LeBel F, Fanaei AE, Ruiz É, Trochu F. Prediction of optimal flow front velocity to minimize void formation in dual scale fibrous reinforcements. Int J Mater Form 2014;7(1):93–116. http://dx.doi.org/10.1007/s12289-012-1111-x.
[18] Michaud V. A review of non-saturated resin flow in liquid composite moulding processes. Transp Porous Media 2016;115(3):581–601. http://dx.doi.org/10.1007/s11242-016-0629-7.
[19] Lundström T, Stenberg R, Bergström R, Partanen H, Birkeland P. In-plane permeability measurements: a nordic round-robin study. Compos Part A: Appl Sci Manuf 2000;31(1):29–43. http://dx.doi.org/10.1016/s1359-835x(99)00058-5.
[20] Arbter R, Beraud JM, Binetruy C, Bizet L, Bréard J, Comas-Cardona S, et al. Experimental determination of the permeability of textiles: a benchmark exercise. Compos Part A: Appl Sci Manuf 2011;42(9):1157–68. http://dx.doi.org/10.1016/j.compositesa.2011.04.021.
[21] Vernet N, Ruiz E, Advani S, Alms JB, Aubert M, Barburski M, et al. Experimental determination of the permeability of engineering textiles: benchmark II. Compos Part A: Appl Sci Manuf 2014;61:172–84. http://dx.doi.org/10.1016/j.compositesa.2014.02.010.
[22] Steenkamer DA, McKnight SH, Wilkins DJ, Karbhari VM. Experimental characterization of permeability and fibre wetting for liquid moulding. J Mater Sci 1995;30(12):3207–15. http://dx.doi.org/10.1007/BF01209239.
[23] Hammond VH, Loos AC. The effects of fluid type and viscosity on the steady-state and advancing front permeability behavior of textile preforms. J Reinf Plast Compos 1997;16(1):50–72. http://dx.doi.org/10.1177/073168449701600105.
[24] Luo Y, Verpoest I, Hoes K, Vanheule M, Sol H, Cardon A. Permeability measurement of textile reinforcements with several test fluids. Compos Part A: Appl Sci Manuf 2001;32(10):1497–504. http://dx.doi.org/10.1016/s1359-835x(01)00049-5.
[25] Orange G, Bessard E, Breard J, Bizet L, Bailleul JL, Comas-Cardona S, et al. Development of composite parts with RTM process based on new high-fluidity thermoplastic polymers. In: 12th International conference on flow processes in composite materials, Enschede, The Netherlands; 2014. <http://www.tech.plym.ac.uk/sme/fpcm/FPCM12%5CExtendedAbstracts%5Cfpcm12_submission_28.pdf>.
[26] Dungan FD, Sastry AM. Saturated and unsaturated polymer flows: microphenomena and modeling. J Compos Mater 2002;36(13):1581–603. http://dx.doi.org/10.1177/0021998302036013179.
[27] Bréard J, Henzel Y, Trochu F, Gauvin R. Analysis of dynamic flows through porous media. Part I: comparison between saturated and unsaturated flows in fibrous reinforcements. Polym Compos 2003;24(3):391–408.
[28] Kim SH, Jung JW, Li MX, Choi SW, Lee WI, Park CH. Unsaturated flow behavior in double-scale porous reinforcement for liquid composite molding processes. J Reinf Plast Compos 2017;36(2):85–97. http://dx.doi.org/10.1177/0731684416671422.
[29] Mortensen A, Wong T. Infiltration of fibrous preforms by a pure metal: Part III. Capillary phenomena. Metall Trans A 1990;21(8):2257–63.
[30] Kistler SF. Hydrodynamics of wetting. In: Berg JC, editor. Wettability, 1st ed., Marcel Dekker Inc., New York: Marcel Dekker Inc; 1993. p. 311–429.
[31] Amico S, Lekakou C. An experimental study of the permeability and capillary pressure in resin-transfer moulding. Compos Sci Technol 2001;61(13):1945–59.
[32] Pucci MF, Liotier P-J, Drapier S. Capillary wicking in a fibrous reinforcement – orthotropic issues to determine the capillary pressure components. Compos Part A: Appl Sci Manuf 2015;77:133–41. http://dx.doi.org/10.1016/j.compositesa.2015.05.031.
[33] Kirinčič S, Klofutar C. A volumetric study of aqueous solutions of poly(ethylene glycol)s at 298.15 K. Fluid Phase Equilib 1998;149(1–2):233–47. http://dx.doi.org/10.1016/s0378-3812(98)00369-0.
[34] Caglar B, Orgéas L, du Roscoat SR, Sozer EM, Michaud V. Permeability of textile fabrics with spherical inclusions. Compos Part A: Appl Sci Manuf 2017;99:1–14. http://dx.doi.org/10.1016/j.compositesa.2017.03.031.
[35] Schindelin J, Arganda-Carreras I, Frise E, Kaynig V, Longair M, Pietzsch T, et al. Fiji: an open-source platform for biological-image analysis. Nature Methods 2012;9(7):676–82. http://dx.doi.org/10.1038/nmeth.2019.
[36] Bruus H. Theorethical Microfluids. oxford mas ed. Oxford University Press; 2008. Also available at: arXiv:1011.1669v3.
[37] Lundström T. The permeability of non-crimp stitched fabrics. Compos Part A: Appl Sci Manuf 2000;31(12):1345–53. http://dx.doi.org/10.1016/S1359-835X(00)00037-3.
[38] Lekakou C, Edwards S, Bell G, Amico SC. Computer modelling for the prediction of the in-plane permeability of non-crimp stitch bonded fabrics. Compos Part A: Appl Sci Manuf 2006;37(6):820–5. http://dx.doi.org/10.1016/j.compositesa.2005.04.002.
[39] Dong S, He H, Jia Y, Wang C, Jiao X. A new structure-related model to predict the permeability of non-crimp fabric preform. J Compos Mater 2012;47(24):3053–63. http://dx.doi.org/10.1177/0021998312462156.
[40] Gebart BR. Permeability of unidirectional reinforcements for RTM. J Compos Mater 1992;26(8):1100–33. http://dx.doi.org/10.1177/002199839202600802.